

# Mass-radius relation of low and very low-mass stars revisited with the VLTI<sup>★</sup>

B.-O. Demory<sup>1</sup>, D. Ségransan<sup>1</sup>, T. Forveille<sup>2</sup>, D. Queloz<sup>1</sup>, J.-L. Beuzit<sup>2</sup>, X. Delfosse<sup>2</sup>, E. Di Folco<sup>1,3</sup>, P. Kervella<sup>3</sup>, J.-B. Le Bouquin<sup>4</sup>, and C. Perrier<sup>2</sup>

<sup>1</sup> Observatoire de Genève, Université de Genève, 51 chemin des Maillettes, 1290 Sauverny, Suisse

<sup>2</sup> Laboratoire d'Astrophysique de Grenoble, 414 rue de la piscine, Domaine Universitaire de Saint Martin d'Hères, 38041 Grenoble, France

<sup>3</sup> LESIA, Observatoire de Paris, CNRS UMR 8109, UPMC, Université Paris Diderot, 5 place Jules Janssen, 92195 Meudon, France

<sup>4</sup> European Southern Observatory, Casilla 19001, Vitacura, Santiago 19, Chile

Received / Accepted

## ABSTRACT

We measured the radii of 7 low and very low-mass stars using long baseline interferometry with the VLTI interferometer and its VINCI and AMBER near-infrared recombiners. We use these new data, together with literature measurements, to examine the luminosity-radius and mass-radius relations for K and M dwarfs. The precision of the new interferometric radii now competes with what can be obtained for double-lined eclipsing binaries. Interferometry provides access to much less active stars, as well as to stars with much better measured distances and luminosities, and therefore complements the information obtained from eclipsing systems. The radii of magnetically quiet late-K to M dwarfs match the predictions of stellar evolution models very well, providing direct confirmation that magnetic activity explains the discrepancy that was recently found for magnetically active eclipsing systems. The radii of the early K dwarfs are well reproduced for a mixing length parameter that approaches the solar value, as qualitatively expected.

**Key words.** Stars: low-mass, very-low-mass–Stars:late-type–Stars: fundamental parameters–Techniques: interferometric

## 1. Introduction

Measuring accurate masses, radii, and luminosities, for low and very low-mass stars has always been observationally challenging. Precise individual masses and radii can be measured through combined photometric and spectroscopic observations of double-lined eclipsing binaries, but to date only ~15 such systems are known with masses under 1 solar mass, and a few of those are too distant and faint for high precision work. Perhaps even more importantly, low mass eclipsing binaries tend, almost by construction, to be fast rotators and hence magnetically very active. Evolutionary models have been found to systematically underestimate the radii of very low mass eclipsing binaries (Torres & Ribas 2002), and the uniformly high activity level of these objects is currently the leading explanation for that discrepancy. Chabrier et al. (2007) find that increased surface spots coverage, and for partly convective stars convection quenching by strong magnetic fields, can inflate the stellar radius by amounts which qualitatively match the observed discrepancy.

Direct tests of that prediction, and validation of the 1-D structural models on objects which better match their assumptions, need radius measurements for slowly rotating and magnetically quiet very low-mass stars. Strong observational selection effects unfortunately ensure that all known eclipsing binaries have sufficiently short orbital periods that they are tidally synchronised, and therefore in turn that all are fast rotators.

Measurements of magnetically quiet slow rotators therefore have to use a different observing technique, long-baseline optical or infrared interferometry. Lane et al. (2001) and Ségransan et al. (2003) both demonstrated 1-5% radius precision for stars that are only partially resolved.

The mass of these single, isolated, stars is not directly accessible, and, strictly speaking, both Lane et al. (2001) and Ségransan et al. (2003) therefore probe the luminosity-radius relation rather than the mass-radius one. Accurate mass and luminosity measurements for M dwarfs (e.g. Ségransan et al. 2000) however demonstrate that their K-band mass-luminosity relation has very low dispersion (Delfosse et al. 2000), and mass is therefore largely interchangeable with absolute K-band luminosity.

Here we present direct angular diameter measurements for seven single K0.5 to M5.5 dwarfs, obtained with the VINCI and AMBER instruments on the Very Large Telescope Interferometer (VLTI) between 2003 and 2008. Section 2 describes those observations, the data analysis, and the angular diameter determination. Section 3 discusses the luminosity-radius and mass-radius relation for very low-mass stars in the light of the new measurements, and compares the empirical relations with theoretical predictions.

## 2. Observations and data analysis

### 2.1. Sample

The target list was largely determined by the capabilities of the VLTI at the time of the observations. The limiting correlated magnitude of the low spectral resolution mode of AMBER on the 1.8m auxiliary telescopes was K=4 in 2007, and improved to K=5.5 in 2008. We consequently selected targets with ap-

Send offprint requests to: Brice-Olivier Demory e-mail: Brice-Olivier.Demory@unige.ch

<sup>★</sup> Based on data collected with the VLTI/VINCI and VLTI/AMBER instruments at ESO Paranal Observatory, programs ID 60.A-9220, 079.D-0565 and 080.D-0653.

parent magnitudes between  $K=2.18$  and  $K=4.38$ . Ongoing improvements to the VLTI infrastructure are expected to provide access to fainter targets. We also computed the expected angular diameters from flux-colour relations and literature photometry, and selected targets with a predicted diameter above 0.9 mas. This translates into a visibility of at most 0.8 on a 128 m baseline in the H-band, as needed to measure diameters to a few % uncertainty with the current amplitude calibration precision of AMBER. One object, GJ 879, was observed as a backup target during an unrelated observing program, and does not fulfill this minimum angular diameter specification.

## 2.2. Observations

### 2.2.1. VINCI Observations

GJ 845 A ( $\epsilon$  Ind), GJ 166 A (DY Eri), GJ 570 A (KX Lib) and GJ 663 A were observed on the ESO Very Large Telescope Interferometer (VLTI) using its commissioning instrument, VINCI (Kervella et al. 2000) with the two 35 cm test siderostats. Table 1 summarises the observation details. VINCI operated in the K-band and used single-mode optical fiber couplers to recombine the light from two telescopes, and modulated the optical path difference around the white light fringe to produce interference fringes. This recombination scheme, first used in the FLUOR instrument (Coude Du Foresto et al. 1998), produces high precision visibility values, thanks to the efficient conditioning of the incoming wavefronts by the single mode fibers, to photometric monitoring of the light coupled into each input fibers, and to fast scanning of the high quality fringes. (Kervella et al. 2004a) extensively describe the data reduction for VINCI.

Our observing strategy alternated sequences of several hundred fringe scans on the target star and on spatially close calibrator stars, to efficiently sample the temporal and spatial structure of the atmospheric and instrumental transfer function. Adherence to this strategy could unfortunately not always be strict, since scientific observations often had to give way to VLTI commissioning activities. For GJ 166 A, in particular, we could only keep three data points since all other measurements had no acceptably close calibrator observations. That target additionally was observed under poorer atmospheric conditions than all other sources, and with two calibrators respectively located 78 and 113 degrees away. It is by far our worst quality measurement, and is thus discarded from this study.

### 2.2.2. AMBER Observations

We used the AMBER (Astronomical Multi-BEam combineR) recombiner of the VLTI to measure the radii of GJ 166 A, GJ 887, *Proxima* (GJ 551) and GJ 879. Table 1 summarizes the observing circumstances. AMBER uses single-mode fibers for wavefront filtering and produces spectrally-dispersed fringes in the J, H, and K near-infrared bands (Petrov et al. 2007). We used the 1.8m-diameter VLT auxiliary telescopes (AT) on the A0-K0-G1 baseline triplet, which at the time of our observations offered the longest available baselines and therefore the highest angular resolution. We selected the low spectral resolution mode (low-JHK) of AMBER, which covers the J, H and K bands with  $R = 30$ , and adopted a 50 ms exposure time. AMBER unfortunately has poor J-band sensitivity, and we detected no fringes in that band. The H-band fringes, on the other hand, probe significantly higher spatial frequencies than the K-

band VINCI would have on the same baselines. We mostly chose to not use the FINITO fringe tracker (Le Bouquin et al. 2008), since our targets were at best close to the H=3 limiting magnitude of FINITO. The fringes would thus not have been sufficiently stabilized to allow much longer integration times and compensate the 80% FINITO levy on the H-band flux.

Since accurate absolute visibility calibration with AMBER had not been demonstrated when we planned the observations, we requested a very conservative observing strategy. Observations of up to four different amplitude calibrators were interleaved with those of each science target, to closely monitor the instrumental and atmospheric transfer function. Those calibrators were chosen from Merand et al. (2004) for angular proximity, well constrained predicted visibilities, and an approximate magnitude and color match to the science targets. The last requirement had to be relaxed somewhat for the M dwarf targets, since we could locate no appropriate M-type calibrators. For those stars we thus used K giant calibrators, which remain fairly close in near-IR colors. Since AMBER had never been used to measure precise angular radii, we chose to reobserve two stars previously measured with VINCI, GJ 551 and GJ 887. VINCI has a well established record of accurate amplitude calibration, and those three stars provide a valuable check on any potential systematics in the AMBER measurements.

GJ 879 was observed as a backup target in very poor atmospheric conditions (seeing FWHM  $> 1.5''$  and  $\tau_0 < 2$ ms), and has the smallest angular radius in our sample (highest  $V^2$ ). Its radius measurement, as a consequence, has significantly larger error bars than that of any other AMBER source.

## 2.3. Data reduction

With angular sizes under 2 mas, our targets are only partially resolved on the longest baselines available for our observations (128 m on the A0-K0 baseline with AMBER, and 140m on the B3-M0 baseline with VINCI). Their squared visibilities  $V^2$  remain above 0.5 in the H-band. We therefore cannot derive their angular diameters from just the location of the first null of the visibility function, and instead need accurate calibration of the visibilities. The very partial resolution, on the other hand, ensures that bandwidth-smearing effects are negligible. At our precision level on the visibilities, accounting for the finite spectral bandwidth would only become necessary for  $V^2$  below 0.3 for VINCI, and well beyond the first visibility null for AMBER.

The end products of both the VINCI and the AMBER pipelines consist of coherence factors ( $\mu^2$ ) together with an internal error estimate on that quantity. The coherence factor is related to the squared visibility,  $V^2$ , through:

$$V_\lambda^2 = \frac{\mu_\lambda^2}{T_\lambda^2}, \quad (1)$$

where  $T^2$  is the squared transfer function of the instrument plus the atmosphere.

Accurate calibration of the absolute squared visibilities therefore critically depends on a well understood transfer function. That function is sensitive to both instrument stability and atmospheric conditions, and can fluctuate during a night. To assess its stability, we calculated the transfer function for every calibrator exposure during a night, disregarding only those datasets for which too few scans/frames passed the reduction pipeline's thresholds to ensure the statistical significance of the resulting

coherence factor measurement. In most cases, the transfer function for each target measurement was evaluated from two different calibrators, providing some control for temporarily deteriorated atmospheric conditions. Using two calibrators also protects against systematics introduced by a poorly chosen calibrator, such as unrecognised binaries. When no calibrator was observed immediately before or after a target point, we adopted the mean of the transfer function for the two nearest calibrators, provided they were observed within 1h of the science measurement. A few observations had to be discarded because no sufficiently close pair of calibrator observations was available. Table 2 and 3 respectively summarise the calibrators' properties for the AMBER and the VINCI observations.

The contribution of the calibration to the visibility error bars accounts for both the statistical uncertainty on the coherence factor and the propagation of the uncertainty on the calibrators' diameters. Since the different  $V^2$  measurements for a given target share any systematic error on the calibrators' diameters, they cannot be considered as fully independent. Those correlations are accounted for in the error bars, using the method described by Perrin (2003). That method is directly applicable to VINCI observations, but needed adaptation for AMBER, as we detail later.

### 2.3.1. VINCI data reduction

We used V. 3.1 of the standard VINCI reduction pipeline (Kervella et al. 2004a). We used the wavelet spectral density (Ségransan et al. 1999) as a visibility estimator, as we found that it more robustly removes pistonned interferograms than the more common Fourier analysis. The commissioning state of the instrument and of the VLTI array often affected the observing strategy, and we had to discard a significant number of measurements for which no calibrator observations were recorded at the same scan frequency. Kervella et al. (2004a) showed, from observations of brighter calibrators, that the squared transfer function of VINCI instrument is stable to within 1.5% during a night. We could therefore average the transfer function measurements from all calibrators observed during one night, and the observed dispersion mainly reflects the statistical errors on these individual measurements. Those are the main source of uncertainties on our final radii obtained with VINCI.

### 2.3.2. AMBER data reduction

**General description** We used the AMBER data reduction pipeline described by Tatulli et al. (2007). After data reduction, we noted structures in the  $V^2$  data obviously resulting from correlations in the dataset presumably due to non-optimal pipeline settings. Indeed, in february 2008, the AMBER TaskForce team (Malbet et al. 2008) made a report of the displacement of the photometric channels with respect to the interferometric channel between 2004 and 2008. Correlations occur on several pixels if those displacements are not correctly calibrated, a step that is achieved through the AMBER standard calibration matrix computation. During our October 2007 observing run, the spectrograph entry slit was tilted and badly focused, thus propagating correlations over 4 to 5 pixels on the detector while AMBER spectral resolution is usually sampled over 2 pixels. We corrected this effect by taking into account integer pixel channel offsets during spectral resifting procedure, to avoid additional correlations to appear during the subtraction of the bad-pixel map at the sub-pixel level. None of our targets had sufficient J-band

flux to offset the poor transmission of AMBER in that band. We therefore discarded the J-band data as well as wavelengths affected by telluric absorption, only keeping the centers of the H and K bands, 1.65 - 1.85  $\mu\text{m}$  and 2.10 - 2.40  $\mu\text{m}$ .

We concatenated all observations of each object (usually 5 sets of 1000 frames) into a single dataset from which we could more robustly select on fringe SNR, to reject pistonned interferograms as well as scans with low flux on one of the two telescopes in a pair. We verified that selecting the best 20% to 75% frames produced similar results, and therefore that the details of the selection do not unduly affect the outcome. Our final was to keep the best 20%, as a trade-off between fringe jitter suppression and increased noise. Selection on an absolute SNR threshold would more effectively reject blurred fringes (which bias down  $V^2$ ) than accepting a specified fraction of the data, but that alternate mode is not available in the current version of the AMBER pipeline. Another limitation of that data reduction package is that it uses a common threshold for all 3 baselines, in spite of their quite different throughputs. Those limitations would become more critical for datasets containing smaller number of scans than we used here.

**Transfer function** As discussed above, a well understood transfer function is critical to measuring absolute visibilities. The stability of the VINCI transfer function is well established, and a wealth of absolute visibilities have been published with that instrument. The reliability of AMBER for absolute  $V^2$  measurements, on the other hand, has been questioned and the stability of the AMBER  $T^2$  needs to be established. Figure 1 shows the squared transfer functions of the 3 AMBER baselines during the night of 27 October 2007. The atmospheric conditions during the first half of the night were representative of Paranal, with a 0.8 arcsec seeing and a coherence time slightly above 3 ms. With a 2 to 4% rms dispersion for both bands on baselines 1 and 3 (90 and 128 m. length respectively) and in K-band for baseline 2 (90 m.), AMBER approaches the stability of the VINCI transfer function. The end of the night had severely degraded atmospheric conditions (2.5 arcsec seeing and 1 ms coherence time), and the transfer function degraded only moderately, except on baseline 2, that had shown a 13% rms dispersion.

**Error bars computation** The reliability of absolute  $V^2$  measured with AMBER has not yet been well established, and evaluating realistic error bars therefore needs close attention. The 16 to 18 spectral channels which we usually kept (7 to 8 in the H-band, and 9 to 10 in the K-band) are measured simultaneously. They therefore share the same atmosphere, as well as any error on the angular diameter of the calibrator(s). If those factors dominate over statistical noise, the individual channels become highly non-independent.

To quantify these correlations between spectral channels, we generalise the formalism developed by Perrin (2003) for a two-channel combiner. For two Gaussian distributions of  $V^2$  series, the correlation coefficient between spectral channel  $k$  and a reference channel,  $r$ , is:

$$\rho_{\lambda_r, \lambda_k} = \frac{\langle (V_{\lambda_r}^2 - \overline{V_{\lambda_r}^2})(V_{\lambda_k}^2 - \overline{V_{\lambda_k}^2}) \rangle}{\sqrt{(V_{\lambda_r}^2 - \overline{V_{\lambda_r}^2})^2 (V_{\lambda_k}^2 - \overline{V_{\lambda_k}^2})^2}}, \quad (2)$$

we computed  $\rho_{\lambda_r, \lambda_k}$  through Monte-Carlo simulations from the mean and variance of  $V_{\lambda_r}^2$  and  $V_{\lambda_k}^2$ . This provides a global corre-

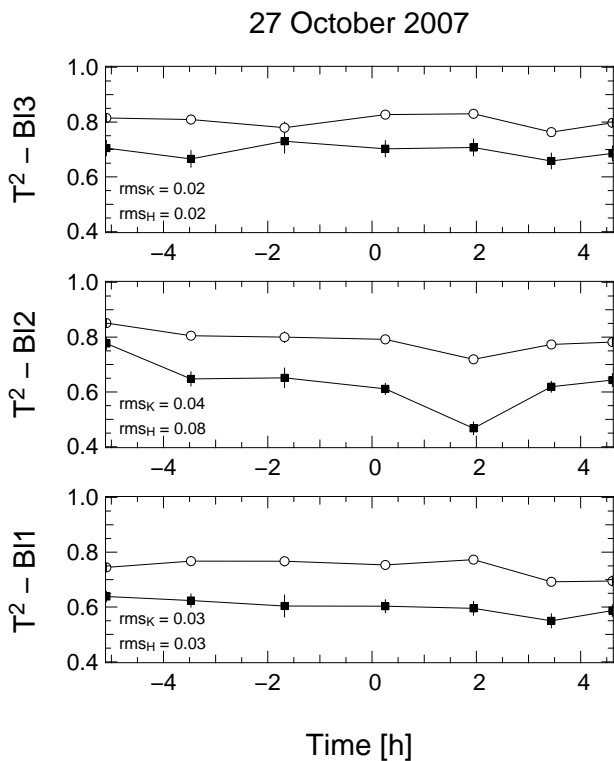


**Fig. 1.** AMBER squared transfer function for Oct 27, 2007. The upper, middle and bottom panel respectively represent baselines 3, 2 and 1. Circles and squares respectively represent the values for the center wavelengths of the K-band ( $2.25\mu\text{m}$ ) and of the H-band ( $1.76\mu\text{m}$ ), The corresponding rms dispersions are reported in each panel.

lation factor for a given band and to estimate amplitude of the error bar that is independent, and then to compute realistic error on the final diameter. As expected, we found that  $V^2$  data in a same spectral band are highly correlated and thus biases the final result if correlations are not taken into account.

Error estimates on final radii obtained with AMBER mainly come from transfer function uncertainties and correlations between squared visibilities. Those factors take more importance as the coherence time degrades.

## 2.4. Data analysis

### 2.4.1. Limb-darkened diameters

At the level of accuracy achieved on the diameter determination for K dwarfs, discrepancy between uniform disk (UD) and limb-darkened disk (LD) is significant. Therefore, we used the non-linear limb-darkening law describing the intensity distribution of the star disk from Claret (2000) :

$$I(\mu) = I(1) \left[ 1 - \sum_{k=1}^4 a_k (1 - \mu^{k/2}) \right], \quad (3)$$

where  $I(1)$  is the specific intensity at the center of the disk,  $\mu = \cos\gamma$ ,  $\gamma$  being the angle between the line of sight and the emergent intensity, and  $a_k$  the limb-darkening coefficients.  $T_{eff}$  and  $\log g$  for each target are shown in table 4, with the corresponding references. We used those parameters, added to the photometric band (K for VINCI, H+K for AMBER) and micro-turbulence velocity (assumed to be  $V_T = 2\text{km/s}$ ), to select

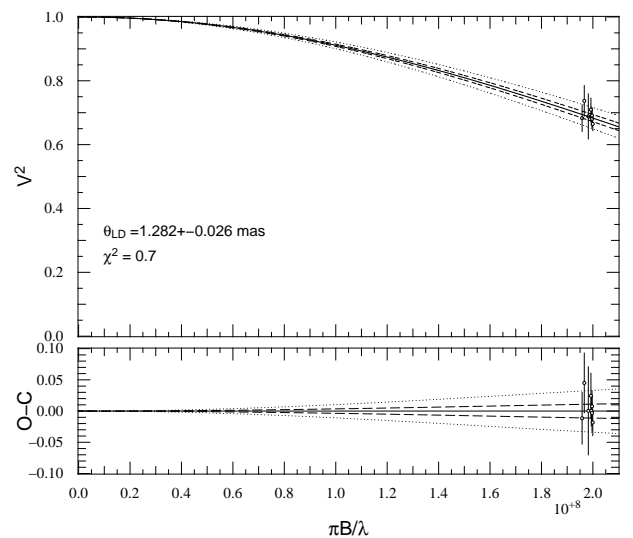


**Fig. 2.** Calibrated squared visibilities from VINCI and best-fit LD disk model (solid) for GJ663A vs. spatial frequencies.  $1-\sigma$  (dash) and  $3-\sigma$  (dot) uncertainties are also indicated.

the corresponding limb-darkening coefficients for the PHOENIX models.

Then, we adjusted a limb-darkened disk that is given by Davis et al. (2000) to the  $V^2$  data :

$$V_{LD,\lambda} = \frac{\int_0^1 d\mu I(\mu) \mu J_0(\pi B \theta_{LD} / \lambda (1 - \mu^2)^{1/2})}{\int_0^1 d\mu I(\mu)} \quad (4)$$

We used the same LD coefficients for H and K bands since corresponding discrepancy has been evaluated at the 0.05% level on the final radius, negligible as compared to the error bar amplitude obtained with AMBER. Uncertainties on the same coefficients due to a slightly different  $T_{eff}$  and  $\log g$  can also be neglected, a 200K change corresponding to a 0.01% on final radius estimate. Table 5 lists the derived UD and LD angular diameters and their corresponding errors for both instruments. Figures 2, 3 and A.1 show  $V^2$  data from VINCI with corresponding fitted LD models for GJ 663 A, GJ 845 and GJ 570 A respectively. Figures 4, 5, A.2 and A.3 show  $V^2$  data from AMBER with corresponding fitted LD models for GJ 887, GJ 166 A, GJ 551 and GJ 879 respectively.

### 2.4.2. Instrument systematics

Assessing systematics is essential to consider when reaching a few percent precision on angular diameters. We thus wanted to check for consistency between both instruments on GJ 887 and GJ 551. The results we obtain are shown in Table 5. Angular diameter determinations are consistent for both instruments. GJ 887 has been observed in optimal conditions in both cases and the agreement is good at  $1-\sigma$  level, as it is for GJ 551. Bracketing each source point with two calibrators allow a better sampling of the transfer function, thus slightly reducing those effects as shown on fig. 1. When good atmospheric conditions are met and a proper calibration applied, systematics on H and K band can be expected to be at 2% level, slightly above VINCI's.

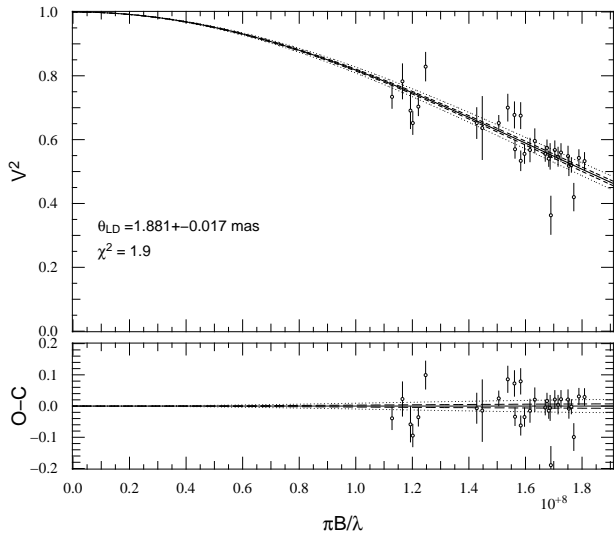


**Fig. 3.** Calibrated squared visibilities from VINCI and best-fit LD disk model (solid) for GJ845 vs. spatial frequencies. 1- $\sigma$  (dash) and 3- $\sigma$  (dot) uncertainties are also indicated.

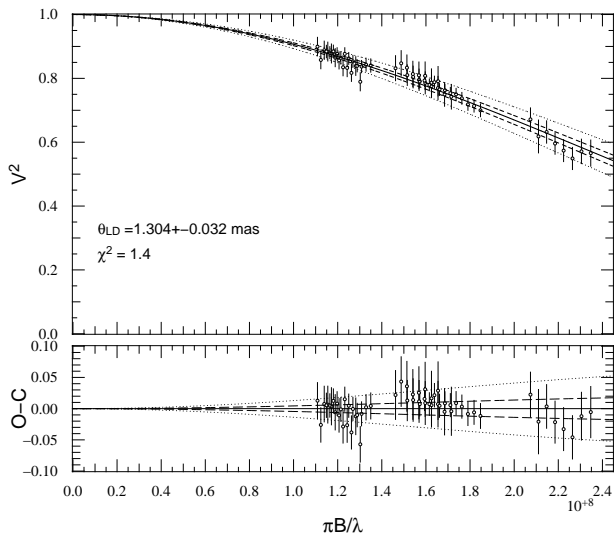


**Fig. 4.** Calibrated squared visibilities from AMBER (low-resolution mode) and best-fit LD disk model (solid) for GJ887 vs. spatial frequencies. 1- $\sigma$  (dash) and 3- $\sigma$  (dot) uncertainties are also indicated. Error bars amplitudes include both correlated and non-correlated errors.

### 3. Discussion

We focussed our study on the low and very low end of the main sequence with spectral types ranging from K0.5 to M5.5. The stars composing our sample cover a wide range of masses - from 0.12 to 0.8  $M_{\odot}$  - which results in different physical conditions affecting their internal structure, the heat transport, as well as their evolution. Their atmosphere chemistry is also strongly affected with the disappearance of true continuum to the benefit of a complex and a high gravity stellar atmosphere with strong molecular absorptions bands. Metallicity and activity also play a role, although we expect it to be a second order effect, at least in the near-infrared. In the following sections, we discuss the implications and constraints brought by our measurements on stellar physics modelling.

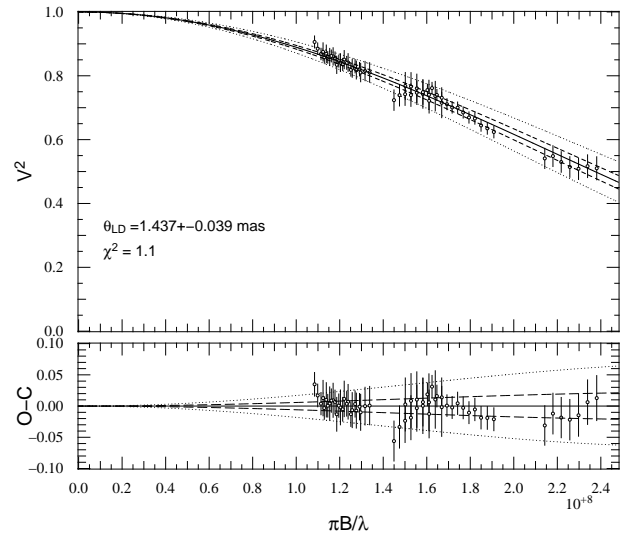


**Fig. 5.** Calibrated squared visibilities from AMBER (low-resolution mode) and best-fit LD disk model (solid) for GJ166A vs. spatial frequencies. 1- $\sigma$  (dash) and 3- $\sigma$  (dot) uncertainties are also indicated. Error bars amplitudes include both correlated and non-correlated errors.

#### 3.1. Luminosity-radius relationship

We have first chosen to compare our results to Baraffe et al. (1998) models, in a luminosity-radius diagram which corresponds to the observables. Indeed, it has the advantage of avoiding the inclusion of the mass-luminosity (hereafter ML) relationship, for which reliability regarding K dwarfs has not been demonstrated yet. Figure 6 shows our VLTI results. Different sets of models are overplotted, ie. for an age of 5 Gyr, featuring different mixing lengths (Böhm-Vitense 1958),  $L_{mix}$  expressed in pressure scale height  $H_p$ , that allow to assess the convective efficiency, as well as two distinct metallicities :  $[M/H] = 0$  and  $[M/H] = -0.5$ .

Baraffe et al. (1998) models are in excellent agreement with our observations in the very low-mass part of the luminosity-radius diagram. The radius determined for *Proxima* (GJ 551) is perfectly reproduced by theory. In this part of the relation, stars are fully convective which greatly simplifies the modelling of heat transport and therefore, our result validates the equation of state used by Baraffe et al. (1998). GJ 887 is an early type M dwarf, located slightly above the boundary of this class of objects. The radius determined for GJ 887 is also in perfect agreement with model predictions. Other measurements from the literature confirms that stellar interior physics for this mass range are well mastered.

At the time of writing this paper, there are relatively few radii measurements that would allow a discussion in the 0.5 - 0.75  $M_{\odot}$  region. 61 Cyg A and B radii have been recently determined by Kervella et al. (2008) and are also well reproduced by theory. We note that Berger et al. (2006) published 6 radii measured with the CHARA array in this part of the diagram. The authors claim discrepancies with models at the 2 to 3  $\sigma$  level. Such large departures from theory have not been observed by other studies. One may note, however, that 5 of the 6 stars measured by Berger et al. (2006) have inflated radii. Those stars were measured with the instrument "CHARA-Classic", a recombiner that does not include a single-mode filtering. Such measurements are prone to systematic calibration errors and indeed, the one star (GJ 15 A) which they measured with "CHARA-FLUOR" (instrument with

single mode filtering) is in excellent agreement with the models. Although a possible explanation, we note that such instrumental effect is expected to result in a uniform dispersion. We decided, however, not to include those results in this discussion.

GJ 205 radius, as measured with VINCI, is about 15% above models. Radial-velocity measurements on this object have not revealed any massive (heavier than a Saturn-mass) companion (X. Bonfils, priv. comm.) that would have induced a lower interferometric visibility, thus a larger radius. Moreover, GJ 205 has not been reported to show significant activity (López-Morales 2007). Nevertheless, this star is more luminous than other known objects belonging to the same spectral class and is probably inflated.

In the upper part of the luminosity-radius relationship, models reproduces the observations provided that larger mixing length are used (such as  $L_{mix} = 1.5H_P$  and  $L_{mix} = 1.9H_P$ ). This part of the relationship may be used to calibrate  $L_{mix}$  provided accurate observational radii and magnitude determination are available.

Figure 7 displays a zoom on this area of the relation.

Unfortunately, GJ 663 A does not appear in the tables nor in the graphs because of the lack of K magnitude measurements. Its measured radius is however shown in table 5 for completeness. It should be noted that some efforts are needed to obtain accurate near-infrared photometry of nearby K dwarfs to tighten the mass-luminosity relation and therefore better constrain theoretical models in the upper part of the luminosity-radius relationship.

### 3.2. Mass-radius relationship

The translation of our direct measurements into a mass-radius diagram requires the use of an empirical ML relationship. We used the relation determined by Delfosse et al. (2000) to compute masses for GJ 887 and GJ 551, and a recent one, by Xia et al. (2008) for the 0.7 to 1.0  $M_{\odot}$  range. This latter study is based on Henry & McCarthy (1993). The ML relationship for stars below 0.6  $M_{\odot}$  is built on a large number of accurate masses and luminosities (Ségransan et al. 2000) and exhibits a very low dispersion in near-infrared. In this part of the mass-luminosity relationship, models reproduce the observations fairly well indicating that both atmosphere and interior physics of very low mass stars are well mastered. The empirical ML relationship above 0.6  $M_{\odot}$  shows a much larger dispersion than for M dwarfs which is related to the modest accuracy of the masses in this mass range. The derivation of masses from absolute magnitude is therefore less accurate than for the lower part of the relation and we adopted an arbitrary error of 5% on masses determination. Those results appear in Table 5. Figure 8 shows our results in a mass-radius (MR) diagram with results from other studies. Five Gyr model isochrones from Baraffe et al. (1998) are represented for different mixing lengths and stellar metallicity.

### 3.3. Stellar properties

#### 3.3.1. Effective temperature

Angular diameter measurements associated with accurate parallax and Johnson photometry allow to derive the star effective temperature. UV to near IR photometry have been obtained from the literature, mostly from Morel & Magnenat (1978). Visual and near-infrared photometry appear in table B.2. We derived effective temperatures, by inverting the surface-brightness empirical relations calibrated by (Kervella et al. 2004b).  $T_{eff}$  val-

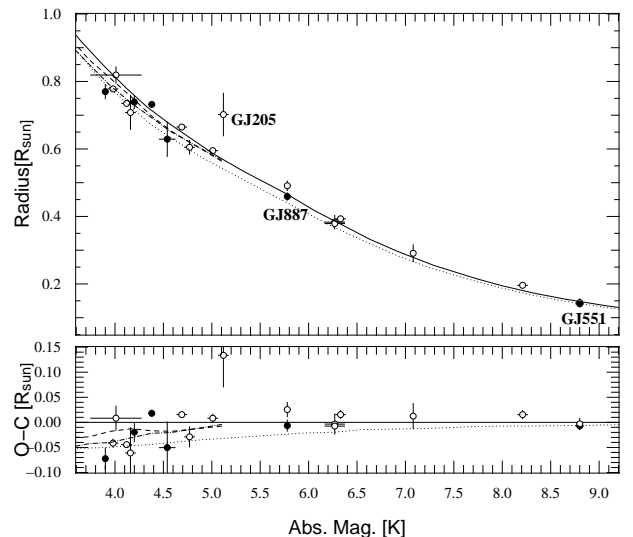


**Fig. 6.** Luminosity-Radius relationship - Single stars radii vs. absolute K magnitudes superimposed on 5 Gyr isochrones theoretical models (Baraffe et al. 1998). Our results from AMBER and VINCI are shown as filled circles. We have also included other stellar radii from the literature determined by interferometry : Berger et al. (2006) for GJ 15 A, Boyajian et al. (2008), di Folco et al. (2007), Kervella et al. (2008), Ségransan et al. (2003) and Lane et al. (2001) as empty circles. Only radii measurements better than 10% are displayed. Different models for 5 Gyr isochrones are also shown : solar metallicity with  $L_{mix} = 1.0H_P$  (solid),  $L_{mix} = 1.5H_P$  (dash) and  $L_{mix} = 1.9H_P$  (dashdot) as well as a metal deficient,  $[M/H] = -0.5$  model with  $L_{mix} = 1.0H_P$  (dot). GJ 205, GJ 887 and GJ 551 that appear in the discussion are labeled.

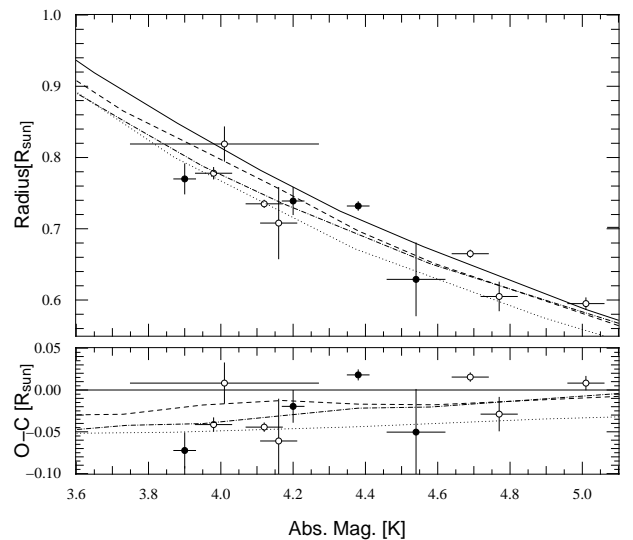


**Fig. 7.** Luminosity-Radius relationship - same as fig. 6, zoomed on the upper part of the diagram.

ues determined through this method are in good agreement with  $T_{eff}$  determined by spectroscopy, both appear in table 5.

#### 3.3.2. Metallicity

Metallicity effects have been mentioned by Berger et al. (2006) to explain the difference between four of his measurements and

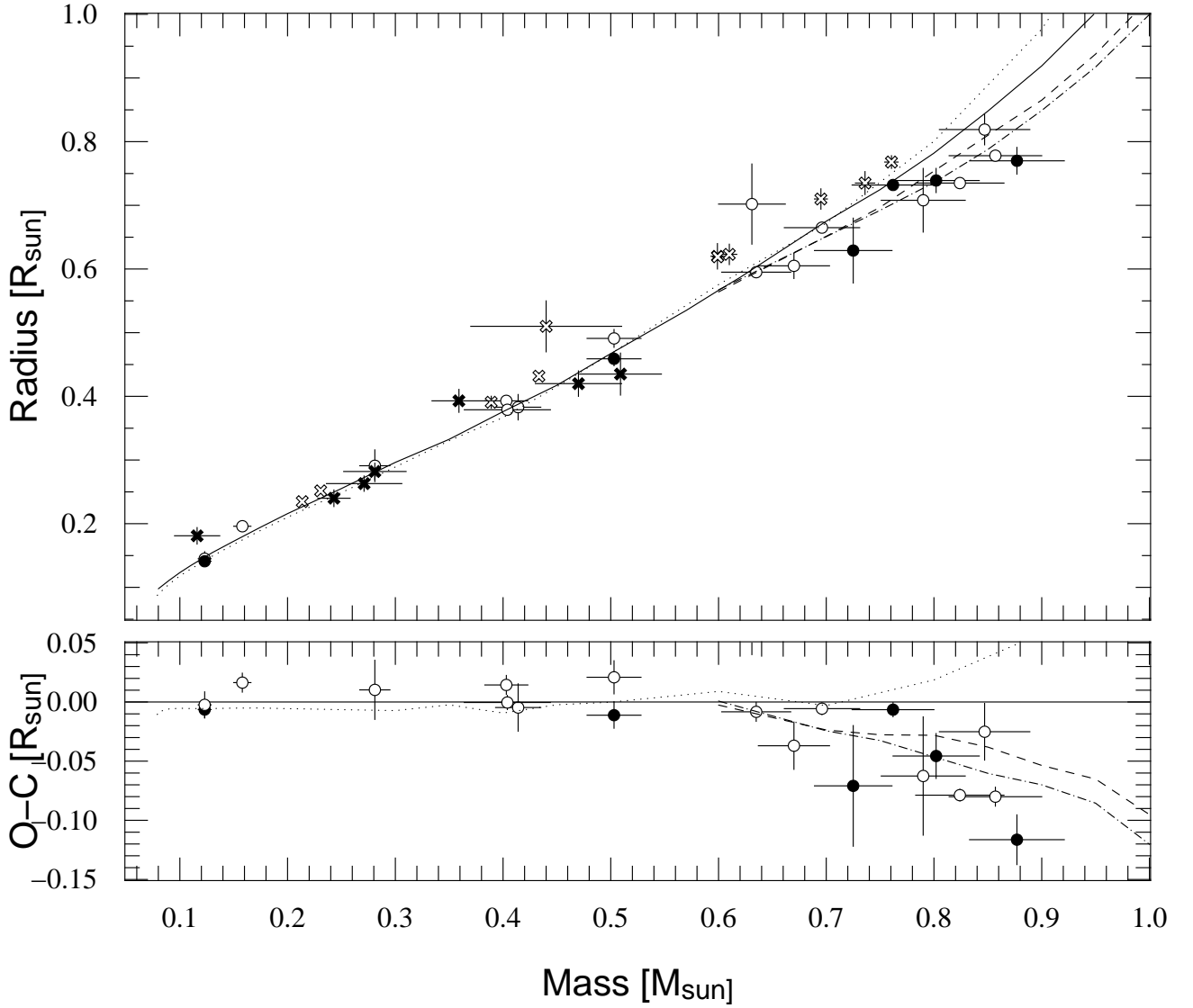


**Fig. 8.** Mass-radius relationship - masses and radii superimposed on 5 Gyr isochrones theoretical models (Baraffe et al. 1998). Our results appear as filled circles. Other long baseline interferometry measurements come from PTI (Lane et al. 2001), VLTI (Ségransan et al. 2003) and CHARA-FLUOR: Boyajian et al. (2008), di Folco et al. (2007), Kervella et al. (2008) and Berger et al. (2006) for GJ15A, all as empty circles. Solar metallicity with  $L_{mix} = 1.0H_P$  (solid),  $L_{mix} = 1.5H_P$  (dash) and  $L_{mix} = 1.9H_P$  (dashdot) are shown as well as a metal deficient,  $[M/H]=-0.5$  model with  $L_{mix} = 1.0H_P$  (dot). Only radii measurements better than 10% are displayed. Solar neighborhood eclipsing binary measurements are represented as empty crosses while OGLE-T transiting binaries are represented in filled crosses. Only residuals from long-baseline interferometry results are displayed.

solar metallicity models. Indeed, the authors claim that missing opacity sources in the models, such as TiO, would explain the models underestimation of stellar radii for some M dwarfs. López-Morales (2007) recently studied the correlation between magnetic activity, metallicity and low-mass stars radii. Based on Berger et al. (2006) measurements, she reach the same conclusion. However, no other instrument (PTI, VINCI, CHARA-FLUOR or AMBER) could confirm this hypothesis except for GJ 205 (VINCI) as explained in Sect. 3.1. Without the "CHARA-Classic" measurements made by Berger et al. (2006), the metallicity-radius diagram for single stars (Fig. 9) no longer shows such correlation.

### 3.3.3. Activity

Close-in eclipsing binaries (EB), for which accurate masses and radii have been measured by several authors such as Torres & Ribas (2002), show significant discrepancies with stellar models (see e.g. Ribas et al. (2008)). Recently, Chabrier et al. (2007) explained those discrepancies by invoking the reduced convective efficiency and starspots coverage of eclipsing binaries. The difference is only observed in mass-radius diagrams (and not in the luminosity-radius diagram) because the slightly lower effective temperature of EB is compensated by a larger radius, only slightly changing the luminosity. This explanation is only meaningful for EB with periods of a few days implying heavy tidal effects, orbital synchronization, and therefore an enhanced activity. This trend is shown on Fig. 8, where EB are represented as empty crosses.

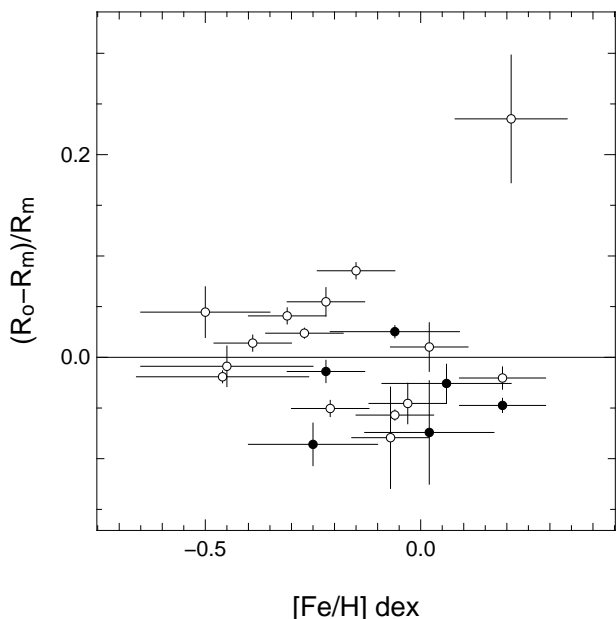


**Fig. 9.** Fractional deviation of single stars radii derived by interferometry from a 5-Gyr,  $L_{mix} = 1.0H_P$  model (Baraffe et al. 1998), vs. stellar metallicity.

However, the same arguments cannot be used in the case of single stars. Rotational velocity is an excellent hint of stellar activity. While low-mass and very low-mass EB are routinely characterised by  $v \sin i$  between 7.11 km/s (CU Cnc B, Ribas (2003) and 129.5 km/s (OGLE BW3 V38A, Maceroni & Montalbán (2004), single stars rarely exceed 3 km/s. We assessed stellar activity for our targets thanks to CORALIE spectra and it indeed appears that all of them do not show an activity comparable with EB ones. Corresponding  $\log R'_{HK}$  and  $v \sin i$  appear in Table 5. Furthermore, activity cannot explain radii discrepancies reported by Berger et al. (2006) since none of those single stars belonging to their sample show high activity levels (López-Morales 2007).

Activity cannot be claimed as the source of deviation in the upper part of the mass-radius relationship for single stars. However, radii of single inactive M dwarfs measured by interferometry are in excellent agreement with models from Baraffe et al. (1998). Thus, discrepancies pointed out by Torres & Ribas (2002) and Ribas (2003) only concern fast rotating stars, confirming the fact that rotation strongly affects the internal structure of those objects.

#### 4. Conclusion

Those new results obtained at the VLTI with its near-infrared instruments, VINCI and AMBER, allow to better constrain the mass-radius relationship for low and very low mass stars. We have shown that AMBER is now able of achieving high quality absolute visibility measurements provided that at least 3 calibrator stars are observed and that a careful data reduction and analysis is conducted. Using VINCI as a benchmark, those results are also shown to be reliable, even if the proposed approach requires a time consuming observing strategy. Assessment of potential systematics as well as realistic error bars estimates have been crucial to compare our results with models in a meaningful way.

Models are in good agreement with the observations, confirming a correct understanding of the underlying physics of low and very low mass stars. The very low-mass regime is almost

adiabatic and thus constraints the equation of state. A small mixing length of  $L_{mix} = 1.0H_P$  leads to a progressive underestimation of radii for early K dwarfs. As expected, the lower convection efficiency in K dwarfs require a significantly greater mixing length to reproduce observed radii of low mass stars.

*Acknowledgements.* We are very grateful to Guy Perrin, Florentin Millour and Gilles Duvert for their advices about AMBER data reduction as well to Stanislav Stefl and Carla Gil for their work as VLTI night astronomers. B.-O.D also would like to thank Fabien Malbet and Guy Perrin for having organized a school devoted to interferometry at Goutelas in 2006. Many thanks also to France Allard and Corinne Charbonnel for fruitful discussions about very low-mass stars atmospheres and interior physics. We thank the anonymous referee for constructive comments on the manuscript. This work benefits from the support of the *Fonds National Suisse de la Recherche Scientifique*. This study has made use of *amdlib 2.2* developed by the Jean-Marie Mariotti Center, supported by INSU (CNRS and Ministère de la recherche, France). This research has made use of the SIMBAD database operated by CDS, Strasbourg, France. This publication makes use of data products from the Two Micron All Sky Survey, which is a joint project of the University of Massachusetts and the Infrared Processing and Analysis Center/California Institute of Technology, funded by the National Aeronautics and Space Administration and the National Science Foundation.

#### References

- Baraffe, I., Chabrier, G., Allard, F., & Hauschildt, P. H. 1998, *Astronomy and Astrophysics*, 337, 403
- Berger, D. H., Gies, D. R., McAlister, H. A., et al. 2006, *The Astrophysical Journal*, 644, 475, (c) 2006: The American Astronomical Society
- Böhm-Vitense, E. 1958, *Zeitschrift für Astrophysik*, 46, 108
- Bonfils, X., Delfosse, X., Udry, S., et al. 2005, *A&A*, 442, 635
- Bordé, P., Coude du Foresto, V., Chagnon, G., & Perrin, G. 2002, *A&A*, 393, 183
- Boyajian, T. S., McAlister, H. A., Baines, E. K., et al. 2008, *ApJ*, 683, 424
- Chabrier, G., Gallardo, J., & Baraffe, I. 2007, *A&A*, 472, L17
- Claret, A. 2000, *A&A*, 363, 1081
- Coude Du Foresto, V., Perrin, G., Ruilier, C., et al. 1998, in Presented at the Society of Photo-Optical Instrumentation Engineers (SPIE) Conference, Vol. 3350, Society of Photo-Optical Instrumentation Engineers (SPIE) Conference Series, ed. R. D. Reasenberg, 856–863
- Cutri, R. M., Skrutskie, M. F., van Dyk, S., et al. 2003, 2MASS All Sky Catalog of point sources. (The IRSA 2MASS All-Sky Point Source Catalog, NASA/IPAC Infrared Science Archive. <http://irsa.ipac.caltech.edu/applications/Gator/>)
- Davis, J., Tango, W. J., & Booth, A. J. 2000, *Monthly Notices RAS*, 318, 387, (c) 2000 The Royal Astronomical Society
- Delfosse, X., Forveille, T., Ségransan, D., et al. 2000, *A&A*, 364, 217
- di Folco, E., Absil, O., Augereau, J.-C., et al. 2007, *A&A*, 475, 243
- Ducati, J. R. 2002, *VizieR Online Data Catalog*, 2237, 0
- Edvardsson, B., Andersen, J., Gustafsson, B., et al. 1993, *A&A*, 275, 101
- Glass, I. S. 1974, *Monthly Notes of the Astronomical Society of South Africa*, 33, 53
- Henry, T. J. & McCarthy, D. W. 1993, *Astronomical Journal (ISSN 0004-6256)*, 106, 773
- Kervella, P., Coude du Foresto, V., Glindemann, A., & Hofmann, R. 2000, in Presented at the Society of Photo-Optical Instrumentation Engineers (SPIE) Conference, Vol. 4006, Society of Photo-Optical Instrumentation Engineers (SPIE) Conference Series, ed. P. Léna & A. Quirrenbach, 31–42
- Kervella, P., Mérand, A., Pichon, B., et al. 2008, *A&A*, 488, 667
- Kervella, P., Ségransan, D., & du Foresto, V. C. 2004a, *A&A*, 425, 1161
- Kervella, P., Thévenin, F., DiFolco, E., & Ségransan, D. 2004b, *A&A*, 426, 297
- Lane, B. F., Boden, A. F., & Kulkarni, S. R. 2001, *The Astrophysical Journal*, 551, L81, (c) 2001: The American Astronomical Society
- Le Bouquin, J.-B., Abuter, R., Bauvir, B., et al. 2008, in Society of Photo-Optical Instrumentation Engineers (SPIE) Conference Series, Vol. 7013, Society of Photo-Optical Instrumentation Engineers (SPIE) Conference Series
- López-Morales, M. 2007, *The Astrophysical Journal*, 660, 732
- Maceroni, C. & Montalbán, J. 2004, *A&A*, 426, 577
- Malbet, F., Duvert, G., Chelli, A., & Kern, P. 2008, *ArXiv e-prints*
- Merand, A., Borde, P., & Foresto, V. C. D. 2004, *New Frontiers in Stellar Interferometry*, 5491, 1185
- Morel, M. & Magnenat, P. 1978, *A&AS*, 34, 477
- Mould, J. R. & Hyland, A. R. 1976, *ApJ*, 208, 399
- Perrin, G. 2003, *A&A*, 400, 1173
- Petrov, R. G., Malbet, F., Weigelt, G., et al. 2007, *A&A*, 464, 1
- Ribas, I. 2003, *A&A*, 398, 239



**Table 1.** Observation log of stars published in this work. AMBER baseline configuration was always A0-K0-G0 (128-90-90)m during our observing runs with this instrument. Some targets were observed during the shared risk observing period (march 2002 - december 2002) of the ESO Very Large Telescope Interferometer (VLTI).

Star	Spectral Type	$m_K$	Instrument	Date	Baseline	DIMM Seeing ["]	Mean $\tau_0$ [ms]				
GJ 663 A	K0V	-	VINCI	13-05-2003	B3-M0 (140m.)	-	-				
				26-05-2003	B3-M0 (140m.)	0.7	5				
				27-05-2003	B3-M0 (140m.)	0.5	7				
				28-05-2003	B3-M0 (140m.)	0.8	6				
GJ 166 A	K0.5V	2.41	AMBER	27-10-2007	A0-K0-G1	1.2	3				
GJ 570 A	K4V	3.06	VINCI	07-04-2003	B3-M0 (140m.)	0.6	4				
				08-04-2003	B3-M0 (140m.)	0.5	6				
				12-04-2003	B3-M0 (140m.)	0.7	6				
				15-04-2003	B3-M0 (140m.)	0.5	9				
				16-04-2003	B3-M0 (140m.)	0.7	5				
				21-04-2003	B3-M0 (140m.)	0.7	4				
				27-04-2003	B3-M0 (140m.)	0.5	3				
				07-05-2003	B3-M0 (140m.)	1.2	2				
				08-05-2003	B3-M0 (140m.)	1.2	3				
				09-05-2003	B3-M0 (140m.)	0.6	7				
				GJ 845 A	K5V	2.18	VINCI	15-09-2002	E0-G1 (66m.)	1.1	2
								16-09-2002	E0-G1 (66m.)	1.0	2
								17-09-2002	E0-G1 (66m.)	0.8	2
10-10-2002	B3-M0 (140m.)	0.9	2								
12-10-2002	B3-M0 (140m.)	1.1	4								
16-10-2002	B3-M0 (140m.)	0.8	7								
17-10-2002	B3-M0 (140m.)	1.2	5								
19-10-2002	B3-M0 (140m.)	0.6	4								
22-10-2002	B3-M0 (140m.)	-	-								
26-10-2002	B3-M0 (140m.)	0.9	3								
GJ 879	K5Vp	3.81	AMBER	03-10-2008	A0-K0-G1	1.4	1				
GJ 887	M0.5V	3.36	AMBER	27-10-2007	A0-K0-G1	1.2	3				
GJ 551	M5.5V	4.38	AMBER	27-02-2008	A0-K0-G1	1.0	3				

**Table 2.** List of calibrator stars used during VINCI runs. Angular diameters come from Bordé et al. (2002) and Merand et al. (2004).

Calibrator	Target	Ang. dist. degrees	Spectral Type	$m_K$	$\theta_{UD}$ K band [mas]
HR 8685	GJ 845	78.3, 19.3	M0III	1.98	2.01±0.02
$\delta$ Phe	GJ 845	31.5	G9III	1.63	2.19±0.02
HR 8898	GJ 845	12.7	M0III	1.81	2.31±0.03
HD 130157	GJ 570 A	2.4	K5III	2.10	2.04±0.02
$\chi$ Sco	GJ 570 A, GJ 663 A	20.6, 20.7	K3III	2.09	2.04±0.02

**Table 3.** List of calibrator stars used during AMBER runs. Angular diameters come from Merand et al. (2004)

Calibrator	Target	Ang. dist. degrees	Spectral Type	$m_K$	$\theta_{UD}$ K band [mas]
HD 25700	GJ 166 A	9.3	K3III	3.16	1.04±0.01
HD 27508	GJ 166 A	9.9	K5III	3.60	0.98±0.01
HD 127897	GJ 551	10.2	K4III	3.82	0.91±0.01
HD 128713	GJ 551	6.4	K0.5II	3.49	0.86±0.01
HD 130227	GJ 551	6.5	K1III	3.59	0.92±0.01
HD 136289	GJ 551	10.1	K3III	3.54	0.94±0.01
HD 204609	GJ 879	19.9	K7III	3.20	1.14±0.02
HD 205096	GJ 879	19.8	K1III	3.82	0.82±0.01
HD 215627	GJ 879, GJ 887	10.3, 6.9	K2III	3.91	0.83±0.01
HD 221370	GJ 887	7.8	K2III	3.61	0.90±0.01
HD 223428	GJ 879	12.4	K1III	3.21	1.07±0.01

Ribas, I., Morales, J. C., Jordi, C., et al. 2008, *Memorie della Societa Astronomica Italiana*, 79, 562

Ségransan, D., Delfosse, X., Forveille, T., et al. 2000, *A&A*, 364, 665

Ségransan, D., Forveille, T., Millan-Gabet, C. P. R., & Traub, W. A. 1999, in *Astronomical Society of the Pacific Conference Series*, Vol. 194, *Working on the Fringe: Optical and IR Interferometry from Ground and Space*, ed.

S. Unwin & R. Stachnik, 290–+

Ségransan, D., Kervella, P., Forveille, T., & Queloz, D. 2003, *A&A*, 397, L5  
Soubiran, C., Bienaymé, O., Mishenina, T. V., & Kovtyukh, V. V. 2008, *A&A*, 480, 91

Tatulli, E., Millour, F., Chelli, A., et al. 2007, *A&A*, 464, 29

Torres, G. & Ribas, I. 2002, *The Astrophysical Journal*, 567, 1140

**Table 4.** Stellar properties. Masses for M-dwarfs are derived from Delfosse et al. (2000) while empirical relation from Xia et al. (2008) is used for K-dwarfs. Metallicity values provided are all directly determined by spectroscopy.

Star	Spect. Type	$M_K$	Teff K	Ref.	Mass [ $M_\odot$ ]	[Fe/H]	Ref.	Derived $T_{eff}$ K	$v \sin i$ km/s	$\log R'_{HK}$	Instr.	Radius [ $R_\odot$ ]
GJ 663 A	K0V	-	-	-	-	-0.20	(3)	4843±134	-	-	VINCI	0.817±0.016
GJ 166 A	K0.5V	3.90±0.02	5201	(3)	0.877±0.044	-0.25	(3)	5269±35	0.78	-4.87	AMBER	0.770±0.021
GJ 570 A	K4V	4.20±0.03	4758	(3)	0.802±0.040	0.06	(3)	4597±101	1.50	-4.48	VINCI	0.739±0.019
GJ 845	K5V	4.38±0.03	4630	(3)	0.762±0.038	-0.06	(3)	4568±59	1.46	-4.56	VINCI	0.732±0.006
GJ 879	K5Vp	4.54±0.08	4574	(3)	0.725±0.036	0.02	(3)	4711 ±134	2.93	-4.27	AMBER	0.629±0.051
GJ 887	M0.5V	5.78±0.03	3626	(1)	0.503±0.025	-0.22	(4)	3797 ±45	-	-	AMBER	0.459±0.011
GJ 551	M5.5V	8.80±0.04	3042	(1)	0.123±0.006	0.19	(2)	3098±56	-	-	AMBER	0.141±0.007

– References:

- For  $T_{eff}$  and [Fe/H]: (1) Ségransan et al. (2003); (2) Edvardsson et al. (1993), (3) CORALIE and (4) Woolf & Wallerstein (2005).
- For  $v \sin i$  and  $\log R'_{HK}$ : CORALIE

**Table 5.** Derived uniform disk and limb-darkened diameters, and stellar radii. Parallaxes are from Hipparcos (van Leeuwen 2007)

Target	Instrument	parallax [mas]	$m_K$	Limb darkening coeff. K band	$\theta_{UD}$ [mas]	$\theta_{LD}$ [mas]
GJ 663 A	VINCI	168.54±0.54	-	[0.79, -0.56, 0.43, -0.15]	1.253±0.025	1.282±0.026
GJ 166 A	AMBER	200.62±0.23	2.39±0.02 (a)	[0.81, -0.53, 0.39, -0.13]	1.405±0.038	1.437±0.039
GJ 570 A	VINCI	171.22±0.94	3.15±0.02 (a)	[0.86, -0.52, 0.37, -0.12]	1.147±0.029	1.177±0.030
GJ 845	VINCI	276.06±0.28	2.18±0.02 (b)	[0.86, -0.53, 0.38, -0.13]	1.834±0.016	1.881±0.017
GJ 879	AMBER	131.42±0.62	3.95±0.08 (a)	[0.86, -0.53, 0.38, -0.13]	0.750±0.066	0.769±0.067
GJ 887	AMBER	305.26±0.70	3.36±0.02 (a)	[1.61, -2.35, 2.00, -0.68]	1.284±0.031	1.304±0.032
GJ 551	AMBER	771.64±2.60	4.38±0.03 (c)	[1.94, -2.80, 2.39, -0.81]	0.990±0.050	1.011±0.052

– References: (a) Morel & Magnenat (1978); (b) Mould & Hyland (1976); (c) 2MASS (Cutri et al. 2003) and (d) Ségransan et al. (2003).

van Leeuwen, F., ed. 2007, Astrophysics and Space Science Library, Vol. 250, Hipparcos, the New Reduction of the Raw Data  
Woolf, V. M. & Wallerstein, G. 2005, MNRAS, 356, 963  
Xia, F., Ren, S., & Fu, Y. 2008, Astrophys Space Sci, 314, 51, (c) 2008: Springer Science+Business Media B.V.

## Appendix A: Online Material - Figures

## Appendix B: Online Material - Tables

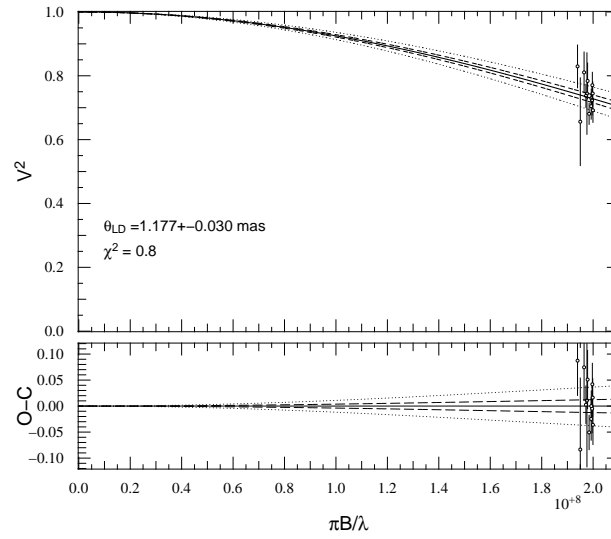


**Fig. A.1.** Calibrated squared visibilities from VINCI and best-fit LD disk model (solid) for GJ570A vs. spatial frequencies.  $1-\sigma$  (dash) and  $3-\sigma$  (dot) uncertainties are also indicated.

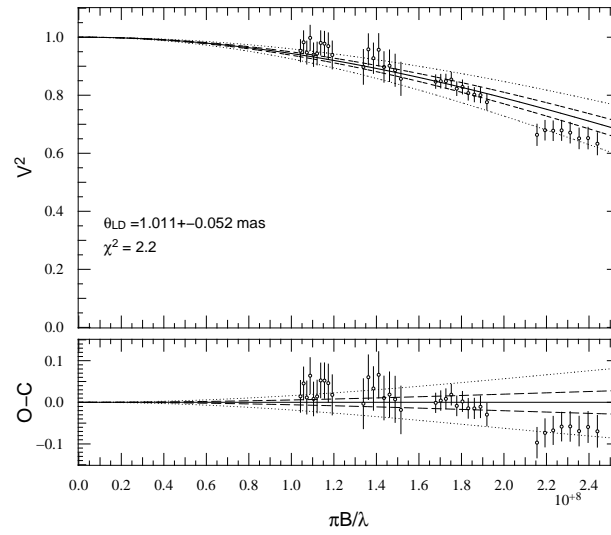


**Fig. A.2.** Calibrated squared visibilities from AMBER (low-resolution mode) and best-fit LD disk model (solid) for GJ551 vs. spatial frequencies.  $1-\sigma$  (dash) and  $3-\sigma$  (dot) uncertainties are also indicated. Error bars amplitudes include both correlated and non-correlated errors.

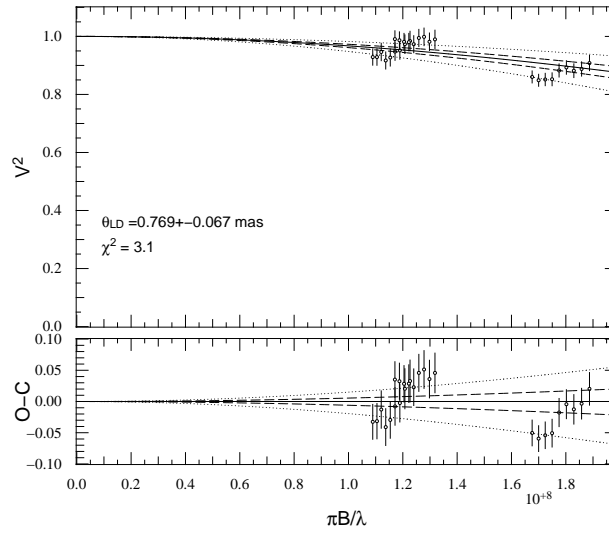


**Fig. A.3.** Calibrated squared visibilities from AMBER (low-resolution mode) and best-fit LD disk model (solid) for GJ879 vs. spatial frequencies. 1- $\sigma$  (dash) and 3- $\sigma$  (dot) uncertainties are also indicated. Error bars amplitudes include both correlated and non-correlated errors.

**Table B.1.** Online material - Angular diameters and linear radii of single low and very-low mass stars from the literature. They are respectively expressed in mas and sun radii.

Star	Spect.	[Fe/H]	Ref. <sub>[Fe/H]</sub>	Instr.	$\theta_{UD}$	$\theta_{LD}$	$R_{in}$	Ref. <sub>interf.</sub>
$\sigma$ Dra	K0V	-0.21	(a)	CHARA	$1.224 \pm 0.011$	$1.254 \pm 0.012$	$0.778 \pm 0.008$	(4)
HR 511	K0V	0.02	(a)	CHARA	$0.747 \pm 0.021$	$0.763 \pm 0.021$	$0.819 \pm 0.024$	(4)
$\epsilon$ Eri	K2V	-0.06	(a)	VINCI	$2.093 \pm 0.029$	$2.148 \pm 0.029$	$0.735 \pm 0.005$	(1)
GJ 105 A	K3V	-0.07	(a)	PTI	$0.914 \pm 0.07$	$0.936 \pm 0.07$	$0.708 \pm 0.050$	(2)
61 Cyg A	K5V	-0.27	(a)	CHARA		$1.775 \pm 0.013$	$0.665 \pm 0.005$	(5)
GJ 380	K7V	-0.03	(a)	PTI	$1.268 \pm 0.04$	$1.155 \pm 0.04$	$0.605 \pm 0.020$	(2)
61 Cyg B	K7V	-0.39	(a)	CHARA		$1.581 \pm 0.022$	$0.595 \pm 0.008$	(5)
GJ 191	M1V	-0.50	(b)	VINCI	$0.681 \pm 0.06$	$0.692 \pm 0.06$	$0.291 \pm 0.025$	(3)
GJ 887	M0.5V	-0.22	(c)	VINCI	$1.366 \pm 0.04$	$1.388 \pm 0.04$	$0.491 \pm 0.014$	(3)
GJ 205	M1.5V	0.21	(c)	VINCI	$1.124 \pm 0.11$	$1.149 \pm 0.11$	$0.702 \pm 0.063$	(3)
GJ 15 A	M2V	-0.45	(d)	PTI	$0.976 \pm 0.016$	$0.988 \pm 0.016$	$0.379 \pm 0.006$	(6)
GJ 411	M1.5V	-0.31	(a)	PTI	$1.413 \pm 0.03$	$1.436 \pm 0.03$	$0.393 \pm 0.008$	(2)
GJ 699	M4Ve	-0.15	(a)	PTI	$0.987 \pm 0.04$	$1.004 \pm 0.04$	$0.196 \pm 0.008$	(2)
GJ 551	M5.5V	0.19	(f)	VINCI	$1.023 \pm 0.08$	$1.044 \pm 0.08$	$0.145 \pm 0.011$	(3)

- Ref. for [Fe/H]: (a) Soubiran et al. (2008); (b) Mould & Hyland (1976); (c) Woolf & Wallerstein (2005); (d) Bonfils et al. (2005); (e) Edvardsson et al. (1993).
- Ref. for interferometric measurements: (1) di Folco et al. (2007); (2) Lane et al. (2001); (3) Ségransan et al. (2003); (4) Boyajian et al. (2008); (5) Kervella et al. (2008); (6) Berger et al. (2006).

**Table B.2.** Apparent magnitudes of stars included in this study. The uncertainty adopted for each apparent magnitude value is given in superscript.

Star	$m_U^{(a)}$	$m_B^{(b)}$	$m_V^{(b)}$	$m_R^{(c)}$	$m_I^{(c)}$	$m_J^{(d)}$	$m_H^{(d)}$	$m_K^{(d)}$	$m_L^{(d)}$
GJ 166 A	$5.69^{0.02}$	$5.25^{0.02}$	$4.43^{0.02}$	$3.72^{0.01}$	$3.27^{0.01}$	$2.91^{0.03}$	$2.46^{0.01}$	$2.39^{0.02}$	$2.30^{0.02}$
GJ 663 A	$5.67^{0.02}$	$5.18^{0.02}$	$4.32^{0.02}$	$3.62^{0.02}$	$3.18^{0.02}$				
GJ 570 A	$7.88^{0.02}$	$6.82^{0.02}$	$5.71^{0.02}$	$4.72^{0.02}$	$4.18^{0.02}$	$3.82^{0.02}$	$3.27^{0.02}$	$3.15^{0.02}$	$3.11^{0.02}$
GJ 845	$6.74^{0.02}$	$5.75^{0.02}$	$4.69^{0.02}$	$3.81^{0.02}$	$3.25^{0.02}$	$2.83^{0.02}$	$2.30^{0.02}$	$2.18^{0.02}$	$2.12^{0.02}$
GJ 879	$8.61^{0.02}$	$7.59^{0.02}$	$6.49^{0.02}$	$5.54^{0.02}$	$4.95^{0.02}$	$4.53^{0.04}$	$4.00^{0.07}$	$3.95^{0.08}$	
GJ 887	$9.99^{0.02}$	$8.83^{0.02}$	$7.35^{0.02}$			$4.20^{0.02}$	$3.60^{0.02}$	$3.36^{0.02}$	$3.20^{0.02}$
GJ 551	$14.56^{0.02}$	$13.02^{0.02}$	$11.05^{0.02}$	$8.68^{0.02}$	$6.42^{0.02}$	$5.33^{0.02}$	$4.73^{0.02}$	$4.36^{0.03}$	$4.04^{0.02}$

– References:

(a) Morel & Magnenat (1978).

(b) Morel & Magnenat (1978), van Leeuwen (2007).

(c) Morel & Magnenat (1978), Ducati (2002).

(d) Morel & Magnenat (1978), Glass (1974), Mould & Hyland (1976), Ducati (2002), Cutri et al. (2003).